

Extracellular potentials generated by axonal projections are shaped by patterns of bifurcations and terminations

Thomas McColgan, Hermann Wagner, Richard Kempter

November 2, 2015

Introduction

Extracellular field potentials (EFPs) are at the heart of many experimental methods used to examine the inner workings of the brain. This includes invasive (Local Field Potentials, Current Source Density, Multiunit Activity) as well as noninvasive (EEG, ECoG, ABR) methods (Nunez and Srinivasan, 2006; Brette and Destexhe, 2012). The origins of these EFPs, especially in cases in which the activity is not clearly attributable to a single cell, is often a matter of debate.

EFPs in the brain were long thought to be primarily synaptic in origin (Buzsáki et al., 2012). As a consequence, many modeling studies focus on the extracellular fields induced by synaptic currents on the dendrites and soma of the postsynaptic neuron (Holt and Koch, 1999; Gold et al., 2006; Lindén et al., 2010, 2011; Einevoll et al., 2013). However, a number of recent data analysis and modeling efforts have revealed that active, non-synaptic membrane currents can play an important role in generating EFPs (Schomburg et al., 2012; Reimann et al., 2013; Anastassiou et al., 2015).

The aim of this study is to understand how the EFP of axons is influenced by the axons anatomical structure. In particular, we aim to explain how typical projection patterns in which an axon bundle widens and then terminates in its projection area affect the EFP. Such axon bundles, sometimes called nerves or fascicles, exist throughout the peripheral and central nervous system of most animals (Nornes and Das, 1972; Goodman et al., 1984; Hentschel and Ooyen, 1999; Kandel et al., 2000). The white matter of the mammalian brain can be viewed as an agglomeration of such bundles (Schüz and Braitenberg, 2002).

It has been shown (Kuokkanen et al., 2010; Denker et al., 2011; Lindén et al., 2011) that with sufficient spatial organization and temporal synchronicity, extracellular fields of axonal and synaptic sources can reach strengths on the order of several mV. Here we extend this finding to include more general axon bundles, including those receiving input with less temporal precision.

We characterize three principal effects of axon bundle structure on the EFP. These effects are elaborations of the properties described in the past (Plonsey, 1977; Gydikov and Trayanova, 1986; Gydikov et al., 1986) for peripheral nerves. We find that the low-frequency components of the EFP are governed by the local density of bifurcations and terminations. The high-frequency components are governed by the local fiber density. Furthermore we show that the low-frequency components exceed the high-frequency components in spatial reach.

We demonstrate these properties using two models of varying complexity, both of them based on a forward model of the extracellular field potential (Holt and Koch, 1999; Gold et al., 2006). The first model includes a detailed multicompartment model of the axon population. The second is an analytically tractable simplification of a generic bundle of axons. Finally, we demonstrate the properties in experimental data using as a set of in-vivo electrophysiological recordings from the barn owl brain stem.

- Some more refs to add: Ray Maunsell 2011, Belluscio 2012, Weiss 2010, rall, Rinzel, Goldwyn, telenzuk

Results

Axonal projections generate a dipole-like field potential To understand the effect of axon geometry on the EFP, we began by simulating a fiber bundle which at first runs at constant diameter and without bifurcations, then reaches a bifurcation zone with an increasing number of fibers, before terminating (Figure 1A). The bundle fibers were stimulated with a background spontaneous rate, upon which a pulse of increased activity was added. The resulting extracellular potential was generated for several locations (Figure 1B) along the axon trunk. The most salient feature of the response traces is a biphasic deflection evoked by the rate pulse. The deflection is visible at all locations, and its peak-to-peak amplitude is indicated by the color code in figures 1A and 1B. Close to the trunk there is also a strong high-frequency noise component, generated by individual spikes. This component diminishes more rapidly in the radial direction, meaning that at larger radial distances the low-frequency component dominates the response.

Frequency components are related to different anatomical features The high-frequency component changes its amplitude in the longitudinal direction in accordance to the local fiber density (Figure 1C). It has an approximately constant amplitude along the nerve trunk and then increases in amplitude as the fiber density is increased by bifurcations. As the fibers terminate and fiber density decreases, so does the amplitude of the high-frequency component.

The low-frequency component shows a different behaviour: it is governed by the local density of bifurcations and terminations (Figure 1D). Along the nerve trunk the fiber density is constant, and the low frequency component is unchanged. As the axon bundle reaches its projection zone, the number of bifurcations increases (Fig 1D), and the low frequency component increases in amplitude (Row 1-5 in Figure 1B). In the middle of the projection zone, the number of bifurcations and terminations cancels out. Correspondingly, the low-frequency component amplitude reaches a local minimum (Row 6 in Figure 1B). As the end of the projection zone approaches, the terminations outweigh the bifurcations, and the amplitude increases, but the polarity is reversed (Rows 7&8 in Figure 1B). As the axon bundle ends, there are no longer any bifurcations or terminations, and the amplitude decays (Row 9 in Figure 1B).

- Examples of similar phenomenology from literature
 - Blot & Barbour
- The low-frequency component exceeds the high-frequency component in reach (**Fig 2**)

The barn owl neurophonic as an example that shows these properties In order to test our model of the extracellular field of axon bundles, we compared it to recordings from the barn owl

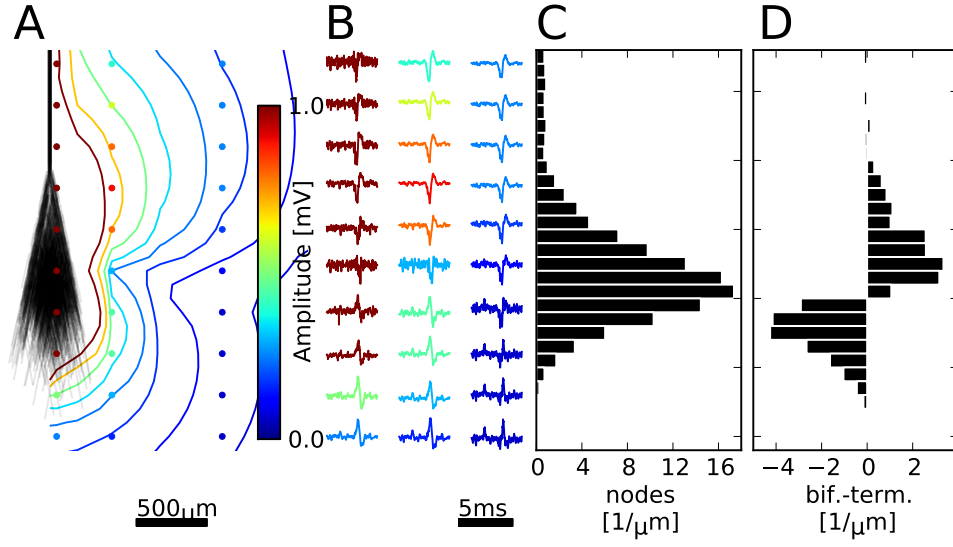


Figure 1: Axonal projections generate a dipole-like extracellular field potential. Extracellular evoked potential due to a pulse of activity in a generic fiber bundle. (A) shows the structure of the bundle, next to (B) EFP responses at various locations, indicated by colored dots. Scaling of traces indicated by colorbar. Relative strength of high-frequency noise relative to the low-frequency pulse decays with distance. The low frequency pulse switches polarity along the nerve bundles termination zone. (C) shows the fiber density overlaid with the strength of the high-frequency EFP component. (D) shows the density of bifurcations and terminations at varying depths.

auditory brain stem. We adjusted the model parameters to match the anatomy and physiology of nucleus laminaris (NL), and set the activation statistics to match measured PSTHs in response to stimulation by a click. We then simulated the resulting EFP at varying depths, corresponding to recording depths in the experiment. The resulting recordings from experiment and simulation are shown in Figure 3.

The simulated EFPs showed several characteristics that are also observed in the data. Firstly, the high-frequency component shows a steady increase in latency along the projections' depth, and has its maximum in amplitude in the middle of NL. The low-frequency component reverses polarity along the depth of NL, and almost vanishes in the middle of NL. This is the same behaviour as shown for the generic axon bundle in the previous section.

It is interesting to note that a similar reversal of polarity in NL has been reported for chicken (Schwarz, 1992), as well as in the mammalian analog to NL, the medial superior olive (Laughlin et al., 2010). The phase reversal in this case has been modeled based on the assumption that the postsynaptic NL and MSO dendrites with their bipolar morphology have a dipolar EFP response [Laughlin et al. (2010); Gold2006Origin]. However, in the owl this dipolar morphology is largely absent (Carr and Konishi, 1990), making dendritic sources unlikely.

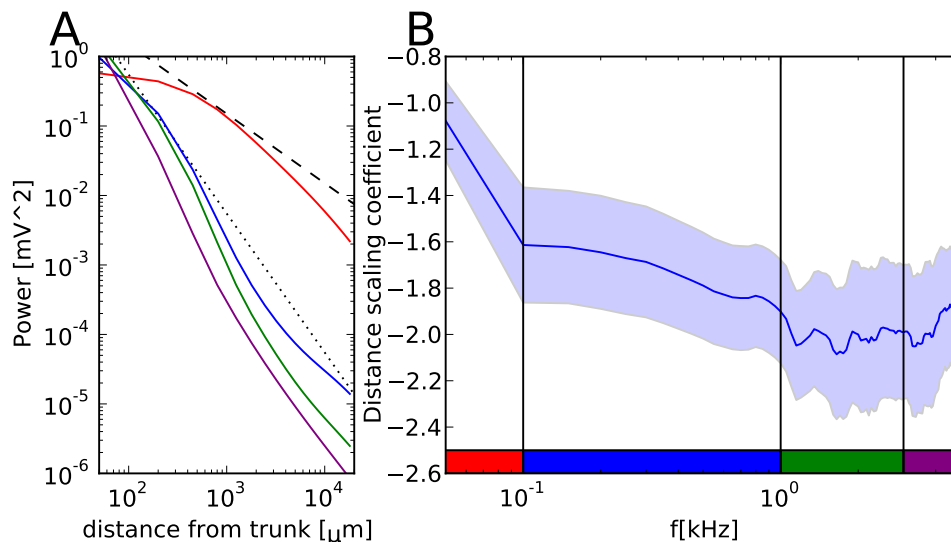


Figure 2: Low-frequency component of the axon bundle EFP exceeds high frequency in reach. (A) shows the behaviour of different spectral components (frequency indicated by colorbar) in a double logarithmic plot. The slope indicates the scaling coefficient in this frequency band. (B) shows this scaling coefficient for different frequencies. Low frequencies have the least negative coefficient, indicating the furthest reach.

Mechanism underlying the observed properties I We begin by looking at the response of a single axon tree to a single spike at various locations along the tree, as shown in Figure 4. This can already give us a rough idea about the origin of the observed polarity reversal.

The extracellular response at a recording location along a continuation of the axon, i.e. not close to a bifurcation or termination, is triphasic (blue trace in Figure 4B). It has been noted that this shape is approximated by the second derivative of the membrane voltage: the first positive peak

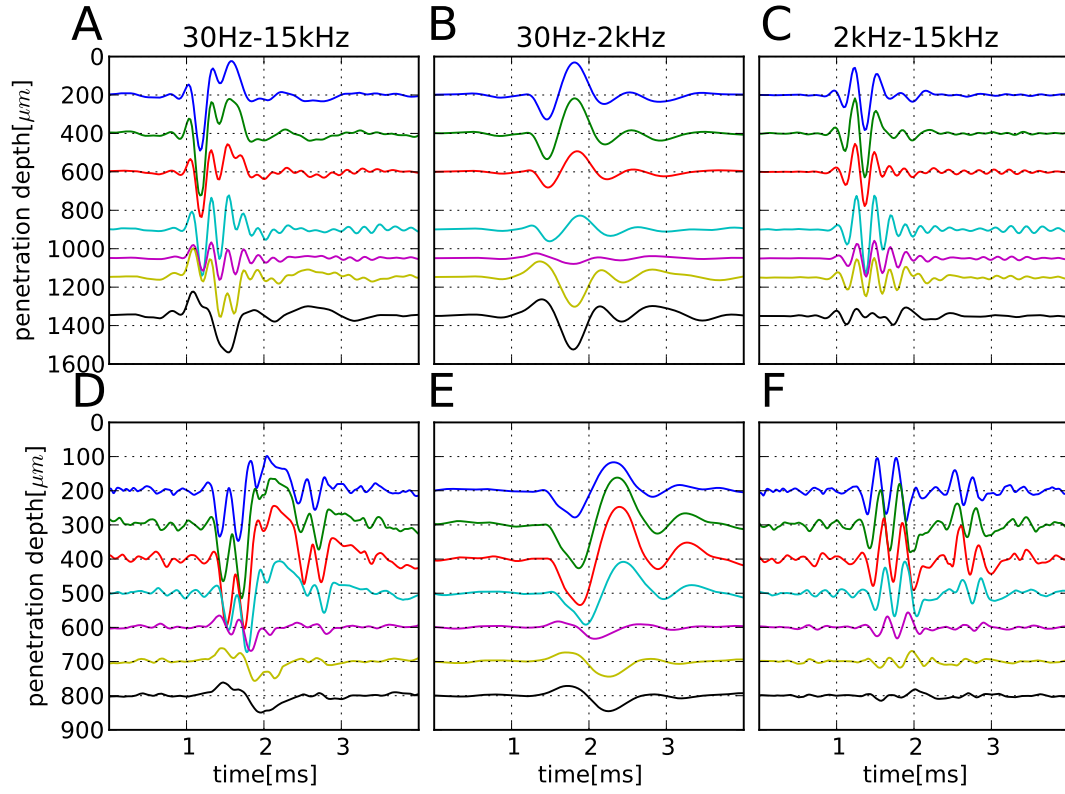


Figure 3: Data from the barn owl shows the expected behaviour predicted by the model. (**A-C**) shows data from the barn owls nucleus laminaris in response to an auditory click stimulus, compared to a simulation of the axonal structure and activation in (**D-F**). The click stimulus induces a pulse of activity in the afferent axon bundle. The low-frequency components (**B** and **E**) show the polarity reversal. The high frequency component (**C** and **F**), does not show such a reversal, but rather shows a steady increase in phase with depth.

is the initial bend to the rising flank of the action potential, the main dip corresponds to the high curvature at the peak of the action potential, and the final, positive peak corresponds to the bend from hyperpolarization to recovery.

The potential near a bifurcation (red trace in Figure 4B) has a more biphasic shape. There is a small initial peak, but the response is dominated by the second, negative and the third, positive peak. This can be understood by comparing the shape to the previous example along a non-bifurcating axon: The initial shape resembles the non-bifurcating case, because the action potential is still mainly within the segments before the bifurcation. As the action potential passes the bifurcation, there are now two instances of the action potential, and the second and third peak are doubled in size, leading to the more biphasic response.

The same reasoning can be applied to the case of the biphasic response at a termination (green trace in Figure 4B): here there is an approaching action potential, leading to an initial positive peak, but as the termination is reached, the current flow ceases, and there is only a reduced second peak, and the third peak, associated with the action potential moving away from the recording location, disappears completely.

The interesting thing to note here is that the potential at the bifurcation and termination are similar in shape, but opposite in polarity. This resembles the observed polarity reversal. It is thus not hard to imagine that this effect is caused by the response being dominated by bifurcations in the early part of NL where the axons branch out, and then by terminations in the later part, where terminations are more prevalent, with the two canceling out in the middle. We will test this intuition in the following by examining the properties of a full bundle of axons in a simplified analytical model.

Mechanism underlying the observed properties II In the case of a simplified one-dimensional axon bundle, the EFP at a given location may be described by the formula $\Phi(\mathbf{r}, t) = [\{n(z) \cdot i_\lambda(z, t)\} * w(a, z)]_z$ (see Methods and appendix). Assuming that the weighting function w tends to 0 for large $|z|$, and with the introduction of the single axon current integral $I_\lambda(z, t) = \int_{-\infty}^z i_\infty(z', t) dz'$, the equation can be split (for a derivation, see appendix) into two components:

$$\Phi(\mathbf{r}, t) = [\{n(z) \cdot I_\lambda(z, t)\} * w'(\rho, z)]_z \quad (1)$$

$$- [\{n'(z) \cdot I_\lambda(z, t)\} * w(\rho, z)]_z \quad (2)$$

In the first component the single axon current integral $I_\lambda(z, t)$ is multiplied by the local density of the fibers n , while the weighting function is replaced by its spatial derivative w' . In the second component, I_λ is multiplied by the derivative of the density n' , but here the weighting function w is unchanged. The functions w and w' are shown in the time and frequency domain in figure 4.

Further inspection of the two components shows an intriguing similarity to the properties of the response observed in the previous sections. The first component is high-pass filtered, and is related to the fiber density, just like ‘noise’ component in Figure 1 and the high-frequency component in the barn owl data and model. The second component is low-pass filtered, and related to the derivative of the fiber density, just like the firing rate pulse related deflection in Figure 1, and the low-frequency component in the barn owl.

The origin of the distinct components will become even clear when considering a minimal example of a fiber density distribution in the shape of a piecewise constant function:

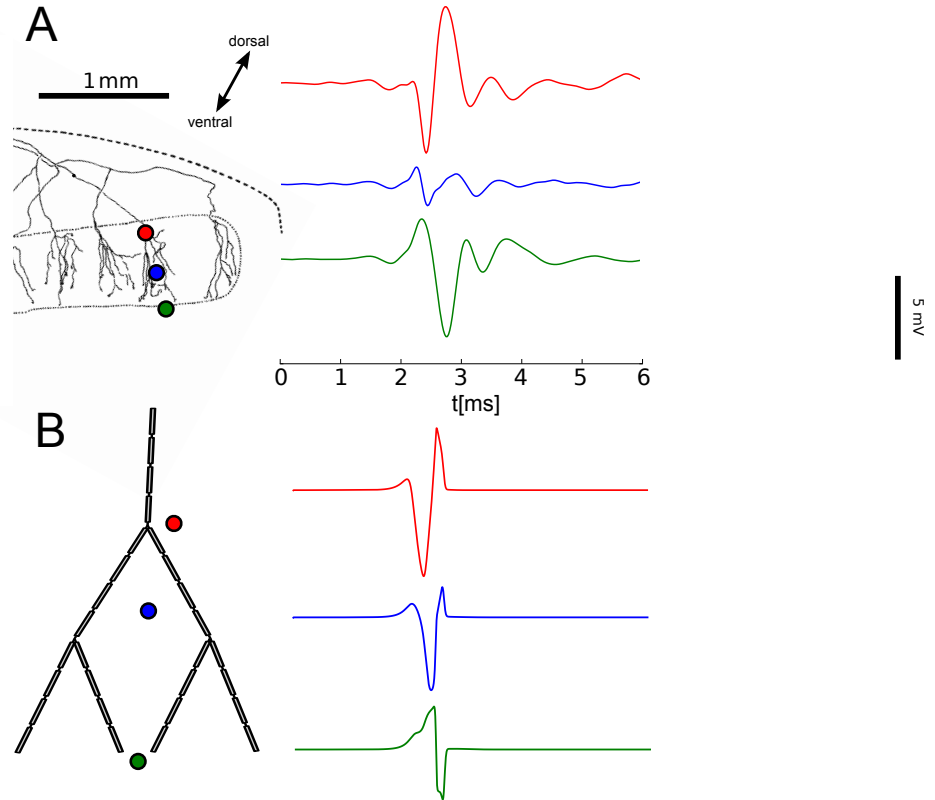


Figure 4: The dipolar behaviour can be understood by examining individual action potentials on a single axon tree. Comparing the low frequency owl data (**A**) to a single axon and action potential in model (**B**) shows a similar behaviour. In particular, the potential at a termination and that at a bifurcation (red and green curves in **B**) are approximately inverted.

$$n(z) = \begin{cases} n_0 & \text{for } z < z_0 \\ n_1 & \text{for } z_0 < z < z_1 \\ 0 & \text{for } z_1 < z \end{cases} \quad (3)$$

In this case, the field potential can be approximated as:

- this may be wrong, double check

$$\Phi(\mathbf{r}, t) \approx -n(z) [w'(\rho, z) * I_\lambda(z, t)]_z \quad (4)$$

$$+ (n_1 - n_0) I_\lambda(z_0, t) w(\rho, z - z_0) \quad (5)$$

$$- n_1 I_\lambda(z_1, t) w(\rho, z - z_1) \quad (6)$$

The first component can be viewed as a filtered version of I_λ , in the same way as shown in section ?? for an infinite axon bundle. In this case, however, the filter is w' , which is an antisymmetric function, and as such a high-pass or band-pass filter which tends to zero for low frequencies (Figure 5B). Thus, this component contributes a local (meaning depending on recording location) version of the signal, with the low frequencies removed.

The timecourse of the second and third component does not depend on I_λ at the recording location z , but rather at the locations of the bifurcations and terminations, z_0 and z_1 , and the amplitudes are attenuated according to w by the distance between these points and the recording location.

If the changes in the membrane currents are slow compared to $(z_1 - z_0)/v$, we can conclude that $I_\lambda(z_0, t) \approx I_\lambda(z_1, t)$, and the second and third component will cancel each other out at a point z_c that fulfills $(n_1 - n_0)w(\rho, z_c - z_0) = n_1 w(\rho, z_c - z_1)$.

- simplify even and move more to methods/appendix.
- explain why this is a dipole
- relate this back to the properties.

Discussion

- Relevance of Findings
 - Interpretation of CSD
 - * Classical CSD: constant fiber density, variable currents
 - * Here: variable fiber density, constant currents
 - Dipole has far field, ABR response?
- Compare to other auditory systems (Chicken NL, MSO)
 - Speculate on functional relevance of polarity shift (a la Rinzel & Goldwyn)
- compare to other fiber bundle systems

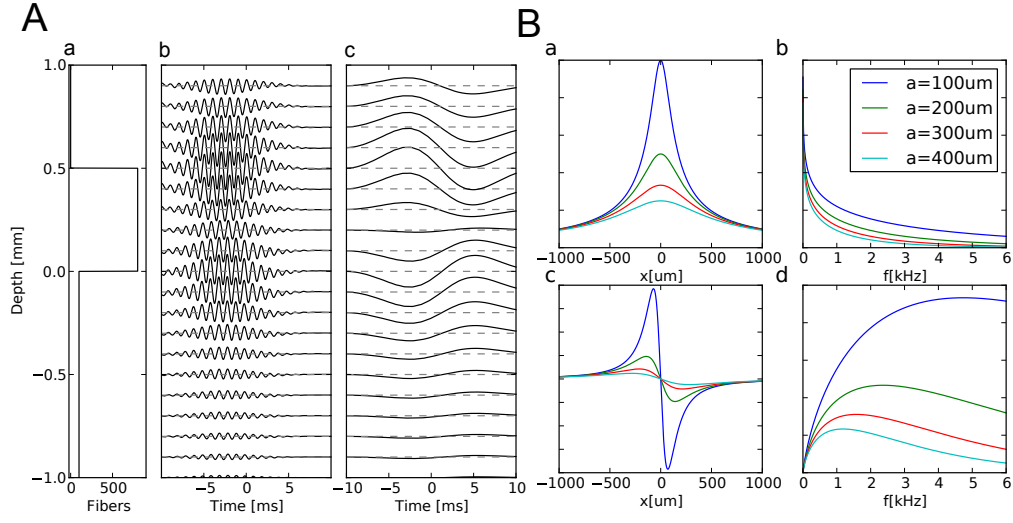


Figure 5: Analytical model of the axon bundle potential explains the effects observed in the numerical model and example data. **(A)** shows the behaviour of a simplified fiber bundle with a piecewise constant fiber density (**Aa**). The high frequency component (**Ab**) shows no polarity reversal, while the high-frequency component (**Ac**) does, as expected from the data and modeling. This can be understood by decomposing the signal into two components. The first component is governed by the bifurcation and termination density, and is filtered by the regular weighting function (**Ba**), which acts as a low-pass filter (**Bb**). The second component is governed by the fiber density, and is filtered by the derivative of the weighting function (**Bc**), which acts as a high- or band-pass filter (**Bd**).

Methods

Experimental recordings

Numerical model

We modeled the axons using NEURON (Hines and Carnevale, 1997; Hines et al., 2009) in a model based on previous work by (refs), including the high and low threshold potassium channels used by (refs). The axon was modeled as a sequence of active nodes and passive myelinated segments. The parameters for the active and passive segments are described in Table 1. Unlike previous models, we included branching axons in our simulations. These were generated by connecting two passive segments to a node, and continuing the alternation of active and passive segment in each resulting branch.

Action potentials were initiated in the axons by injecting a current pulse into the first node of Ranvier of the axon. The times of the injections were chosen by drawing from an inhomogeneous Poisson distribution based on the firing statistics of NM units in response to a given stimulus.

- Split barn owl and general axon bundle

Axon branching patterns were generated procedurally, **better wording** starting with the root segment, placed at the border of NL. In order to avoid artifacts from the current pulse injection and to simulate the fiber tract leading up to NL, a sequence of 10 active and passive segments without bifurcations was added before the root. To this root, segments were appended iteratively. Before adding a segment, a decision whether to branch or terminate an axon was drawn from a probability distribution dependent on the dorsoventral depth of the end of the previous segment. These probability distributions were modeled as logistic functions with the parameters adjusted to roughly match the numbers of branchings and terminations found in the tracings shown in publications such as Carr and Konishi (1990). This meant that an initial phase of bifurcations was followed by a phase of terminations, with the probability of termination reaching 100% at the end of NL.

The simulations of these axons yielded the membrane currents, from which we calculated the extracellular fields. The procedure for this is described in detail by Gold et al. (2006), among others. Briefly, the extracellular medium is assumed to be a homogeneous volume conductor with conductivity σ_e , and a quasi-static approximation of the electrical field potential ϕ is made. The extracellular potential due to a current distribution $i(\mathbf{r}, t)$ is then governed by the equation $\Delta\phi = \frac{1}{\sigma_e}i(\mathbf{r}, t)$, with Δ denoting the Laplace operator. If the currents i are constrained to a volume V , this equation has the solution:

$$\phi(\mathbf{r}, t) = \frac{1}{4\pi\sigma_e} \int_V \frac{i(\mathbf{r}', t)}{|\mathbf{r} - \mathbf{r}'|} d\mathbf{r}' \quad (7)$$

Since the currents through the myelinated segments were negligible, and the nodes of Ranvier are small, we used the point source approximation of only the node currents, and did not include the line source approximation used by Holt and Koch (1999).

parameter	value
g_{Na}	0.8 S/cm ²
g_{KLVA}	0.1 S/cm ²
g_{KHVA}	1.5 S/cm ²
C_{mem}	1.0 $\mu\text{F}/\text{cm}^2$

Table 1: Model Parameters **add: leak conductance, myelin parameters, extracellular conductivity sizes**

Simplified axon bundle model

We define the spatial dimension in cylindrical coordinates $\mathbf{r} = (\rho, \varphi, z)$ such that z is the dorsoventral direction, increasing from dorsal to ventral, and $z = 0$ is the dorsal border of NL. We further define $\hat{\mathbf{e}}_z$ as the unit vector in z direction, and $\hat{\mathbf{e}}_\rho$ as an arbitrary unit vector perpendicular to the z direction.

Let us first consider a simple model axon that extends infinitely on both sides and in a straight line from the dorsal direction into NL, and at 0 in the remaining coordinates. Furthermore, we consider a single action potential propagating along this axon. This axon then has a non-zero current density only at $\rho = 0$, which we denote $i_\infty(z, t)$, meaning that in this case $i(\mathbf{r}, t) = \delta(\rho)i_\infty(z, t)$. Applying this to equation 7, corresponding response $\kappa_\infty(\mathbf{r}, t)$ of an action potential propagating through such a line-axon is then

$$\kappa_\infty(\mathbf{r}, t) = \frac{1}{4\pi\sigma_e} \int_V \frac{\delta(\rho')i_\infty(z', t)}{|\mathbf{r} - \mathbf{r}'|} d\mathbf{r}' \quad (8)$$

$$= \frac{1}{4\pi\sigma_e} \int_{-\infty}^{\infty} \frac{i_\infty(z', t)}{|\mathbf{r} - z'\hat{\mathbf{e}}_z|} dz' \quad (9)$$

We will call this response a spike kernel because it will take the role of an integral kernel in the following.

Due to the rotational symmetry, the kernel at a distance ρ from the axon, regardless of φ , can then be described by

$$\kappa_\infty(\mathbf{r}, t) = \frac{1}{4\pi\sigma_e} \int_{-\infty}^{\infty} \frac{i_\infty(z', t)}{|(z - z')\hat{\mathbf{e}}_z + \rho\hat{\mathbf{e}}_\rho|} dz' \quad (10)$$

$$= \frac{1}{4\pi\sigma_e} \int_{-\infty}^{\infty} \frac{i_\infty(z', t)}{\sqrt{(z - z')^2 + \rho^2}} dz' \quad (11)$$

Equation 10 has the form of a convolution with a weighting function w :

$$w(\rho, z) = \frac{1}{4\pi\sigma_e} \frac{1}{\sqrt{z^2 + \rho^2}} \quad (12)$$

The convolution can then be written as:

$$\kappa_\infty(\mathbf{r}, t) = [i_\infty(z, t) * w(\rho, z)]_z \quad (13)$$

with the operator $[\cdot * \cdot]_z$ denoting the convolution with respect to the variable z .

The simplest model of a terminating axon will be a semi-infinite axon, where the membrane current flow is simply set to zero beyond the termination point z_{term} . Using the Heaviside step function H we find kernel κ_{term} of a spike in a terminating axon:

$$\kappa_{\text{term}}(\mathbf{r}, t) = [\{H(z_{\text{term}} - z) \cdot i_\infty(z, t)\} * w(\rho, z)]_z \quad (14)$$

Similarly, the model of a bifurcating axon would be one in which the current flow after the bifurcation point z_{bif} is double that of the single infinite fiber.

$$\kappa_{\text{bif}}(\mathbf{r}, t) = [\{(1 + H(z - z_{\text{bif}})) \cdot i_\infty(z, t)\} * w(\rho, z)]_z \quad (15)$$

This places the child branches in superposition at $\rho = 0$, which is a useful approximation for small branching angles.

Approximating terminations and bifurcations in this way disregards the boundary effects that may appear due to the conservation of charge and the inability of charge to flow beyond the termination. However, since the integral over i_∞ is zero for realistic action potentials, the conservation of charge is maintained in the long run.

In more general terms, a coherently stimulated axon bundle with terminations and bifurcations along its path can be described by the number of individual fibers $n(z)$ at any depth. The extracellular potential κ_b of such a bundle in which the action potential is initiated at the same time and location is then given by

$$\kappa_b(\mathbf{r}, t) = [\{n(z) \cdot i_\infty(z, t)\} * w(\rho, z)]_z \quad (16)$$

If we want to calculate the combined field of many axons and action potentials, we can do so by linearly summing the individual axon fields.

If all axons in the bundle are driven with the same the mean firing rate $\lambda(t)$, which might be modulated in time, the field potential $\Phi(\mathbf{r}, t)$ in response to this firing rate will be the (temporal) convolution of the firing rate with the response of the bundle to a coherent spike in all axons:

$$\Phi(\mathbf{r}, t) = [\kappa_b(\mathbf{r}, t) * \lambda(t)]_t \quad (17)$$

Substituting equation 16 into equation 17, and taking advantage of the fact that only i_∞ and λ depend on t gives

$$\Phi(\mathbf{r}, t) = [[\{n(z) \cdot i_\infty(z, t)\} * w(\rho, z)]_z * \lambda(t)]_t \quad (18)$$

$$= [\{n(z) \cdot [i_\infty(z, t) * \lambda(t)]_t\} * w(\rho, z)]_z \quad (19)$$

With the average current in a single infinite fiber stimulated with λ , which we will denote it with $i_\lambda(z, t) := [i_\infty(z, t) * \lambda(t)]_t$ this gives us

$$\Phi(\mathbf{r}, t) = [\{n(z) \cdot i_\lambda(z, t)\} * w(a, z)]_z \quad (20)$$

Bibliophraphy

Anastassiou CA, Perin R, Buzsáki G, Markram H, Koch C (2015) Cell type- and activity-dependent extracellular correlates of intracellular spiking. *Journal of Neurophysiology* 114:608–623 Available at: <http://dx.doi.org/10.1152/jn.00628.2014>.

Brette R, Destexhe A eds. (2012) *Handbook of Neural Activity Measurement*. Cambridge: Cambridge University Press. Available at: <http://dx.doi.org/10.1017/cbo9780511979958>.

Buzsáki G, Anastassiou CA, Koch C (2012) The origin of extracellular fields and currents — EEG, ECoG, LFP and spikes. *Nature Reviews Neuroscience* 13:407–420 Available at: <http://dx.doi.org/10.1038/nrn3241>.

Carr CE, Konishi M (1990) A circuit for detection of interaural time differences in the brain stem of the barn owl. *The Journal of Neuroscience* 10:3227–3246 Available at: <http://www.jneurosci.org/content/10/10/3227.abstract>.

Denker M, Roux S, Lindén H, Diesmann M, Riehle A, Grün S (2011) The Local Field Potential Reflects Surplus Spike Synchrony. *Cerebral Cortex* 21:2681–2695 Available at: <http://dx.doi.org/10.1093/cercor/bhr040>.

Einevoll GT, Kayser C, Logothetis NK, Panzeri S (2013) Modelling and analysis of local field potentials for studying the function of cortical circuits. *Nature Reviews Neuroscience* 14:770–785 Available at: <http://dx.doi.org/10.1038/nrn3599>.

Gold C, Henze DA, Koch C, Buzsáki G (2006) On the origin of the extracellular action potential waveform: A modeling study. *Journal of neurophysiology* 95:3113–3128 Available at: <http://dx.doi.org/10.1152/jn.00979.2005>.

Goodman CS, Bastiani MJ, Doe CQ, Lac S du, Helfand SL, Kuwada JY, Thomas JB (1984) Cell recognition during neuronal development. *Science (New York, NY)* 225:1271–1279 Available at: <http://view.ncbi.nlm.nih.gov/pubmed/6474176>.

Gydikov A, Gerilovsky L, Radicheva N, Trayanova N (1986) Influence of the muscle fibre end geometry on the extracellular potentials. 54:1–8 Available at: <http://dx.doi.org/10.1007/bf00337110>.

Gydikov AA, Trayanova NA (1986) Extracellular potentials of single active muscle fibres: Effects of finite fibre length. 53:363–372 Available at: <http://dx.doi.org/10.1007/bf00318202>.

Hentschel HGE, Ooyen A van (1999) Models of axon guidance and bundling during development. *Proceedings of the Royal Society of London B: Biological Sciences* 266:2231–2238 Available at: <http://dx.doi.org/10.1098/rspb.1999.0913>.

Hines ML, Carnevale NT (1997) The NEURON Simulation Environment. *Neural Computation* 9:1179–1209 Available at: <http://dx.doi.org/10.1162/neco.1997.9.6.1179>.

Hines ML, Davison AP, Muller E (2009) NEURON and Python. *Frontiers in neuroinformatics* 3 Available at: <http://dx.doi.org/10.3389/neuro.11.001.2009>.

Holt GR, Koch C (1999) *Electrical Interactions via the Extracellular Potential Near Cell Bodies*.

Journal of Computational Neuroscience 6:169–184 Available at: <http://dx.doi.org/10.1023/a:1008832702585>.

Kandel ER, Schwartz JH, Jessell TM, Others (2000) Principles of neural science. McGraw-Hill New York.

Kuokkanen PT, Wagner H, Ashida G, Carr CE, Kempter R (2010) On the origin of the extracellular field potential in the nucleus laminaris of the barn owl (*Tyto alba*). Journal of neurophysiology 104:2274–2290 Available at: <http://dx.doi.org/10.1152/jn.00395.2010>.

Laughlin MM, Verschooten E, Joris PX (2010) Oscillatory Dipoles As a Source of Phase Shifts in Field Potentials in the Mammalian Auditory Brainstem. The Journal of Neuroscience 30:13472–13487 Available at: <http://dx.doi.org/10.1523/jneurosci.0294-10.2010>.

Lindén H, Pettersen K, Einevoll G (2010) Intrinsic dendritic filtering gives low-pass power spectra of local field potentials. Journal of computational neuroscience 29:423–444 Available at: <http://dx.doi.org/10.1007/s10827-010-0245-4>.

Lindén H, Tetzlaff T, Potjans TC, Pettersen KH, Grün S, Diesmann M, Einevoll GT (2011) Modeling the Spatial Reach of the LFP. Neuron 72:859–872 Available at: <http://dx.doi.org/10.1016/j.neuron.2011.11.006>.

Nornes HO, Das GD (1972) Temporal pattern of neurogenesis in spinal cord: cytoarchitecture and directed growth of axons. Proceedings of the National Academy of Sciences of the United States of America 69:1962–1966 Available at: <http://view.ncbi.nlm.nih.gov/pubmed/4114859>.

Nunez PL, Srinivasan R (2006) Electric Fields of the Brain. Oxford University Press. Available at: <http://dx.doi.org/10.1093/acprof:oso/9780195050387.001.0001>.

Plonsey R (1977) Action potential sources and their volume conductor fields. Proceedings of the IEEE 65:601–611 Available at: <http://dx.doi.org/10.1109/proc.1977.10539>.

Reimann MW, Anastassiou CA, Perin R, Hill SL, Markram H, Koch C (2013) A Biophysically Detailed Model of Neocortical Local Field Potentials Predicts the Critical Role of Active Membrane Currents. Neuron 79:375–390 Available at: <http://dx.doi.org/10.1016/j.neuron.2013.05.023>.

Schomburg EW, Anastassiou CA, Buzsáki G, Koch C (2012) The Spiking Component of Oscillatory Extracellular Potentials in the Rat Hippocampus. The Journal of Neuroscience 32:11798–11811 Available at: <http://dx.doi.org/10.1523/jneurosci.0656-12.2012>.

Schüz A, Braitenberg V (2002) The Human Cortical White Matter. In: Cortical areas (Schüz A, ed), pp 377–386. Abingdon, UK: Taylor & Francis. Available at: http://dx.doi.org/10.4324/9780203219911/_chapter/_16.

Schwarz DW (1992) Can central neurons reproduce sound waveforms? An analysis of the neurophonic potential in the laminar nucleus of the chicken. The Journal of otolaryngology 21:30–38 Available at: <http://view.ncbi.nlm.nih.gov/pubmed/1564747>.